© 2019 Society for Industrial and Applied Mathematics

HYBRIDIZED CutFEM FOR ELLIPTIC INTERFACE PROBLEMS[*]

ERIK BURMAN[†], DANIEL ELFVERSON[‡], PETER HANSBO[§], MATS G. LARSON[‡],
AND KARL LARSSON[‡]

Abstract. We design and analyze a hybridized cut finite element method for elliptic interface problems. In this method very general meshes can be coupled over internal unfitted interfaces, through a skeletal variable, using a Nitsche type approach. We discuss how optimal error estimates for the method are obtained using the tools of cut finite element methods and prove a condition number estimate for the Schur complement. Finally, we present illustrating numerical examples.

1. Introduction. The solution of heterogeneous problems, for instance, problems where some physical parameter has important variation within the computational domain, remains a challenging problem in computational science. Indeed special care must be taken in the design of methods to ensure that efficiency and accuracy do not degenerate in the presence of high contrast inclusions. An additional layer of complexity is added if the internal structure, e.g., the position of the inclusion, is one of the problem unknowns and domain boundaries or internal interfaces must be modified during the computation. In this situation it is an advantage if remeshing of the domain can be avoided, while the equations still are solved accurately on a variety of configurations [39, 6]. When one interface separates two computational domains and the problem size is moderate it is reasonable to use a monolithic solution strategy. However, as the number of inclusions increases it becomes advantageous to resort to domain decomposition so that the problem can be solved in parallel.

Recently there has been a surge of activity in the design and analysis of hybridized methods, that is, nonconforming methods that have different approximating polynomials defined in the bulk of the elements and on the skeleton of the computational mesh. The skeleton variable plays the role of a mortar variable, for either a Neumann or a Dirichlet trace. Typically the interior degrees of freedom of each cell can easily be eliminated using static condensation, thereby reducing the size of the linear system. This is particularly appealing for high order approximation methods where each volume element hosts a relatively large number of degrees of freedom. An important feature of hybridized methods is that they allow for fairly general

[†]Department of Mathematics, University College London, London, WC1E 6BT, UK (e.burman@ucl.ac.uk).

[‡]Department of Mathematics and Mathematical Statistics, Umeå University, SE-901 87 Umeå, Sweden (daniel.elfverson@umu.se, mats.larson@umu.se, karl.larsson@umu.se).

[§]Department of Mechanical Engineering, Jönköping University, SE-551 11 Jönköping, Sweden (peter.hansbo@ju.se).

element shapes and there exists an important literature on methods defined on general polygonal/polyhedral meshes. Examples of such methods include the hybridized discontinuous Galerkin method [16], the virtual element method [1], and the hybridized high order method [17]. In many cases these methods are closely related (see [15] and references therein).

In this contribution we design a hybridized finite element method within the cut finite element method (CutFEM) paradigm; see [7, 4]. This means that the computational mesh is independent of the geometry and internal interfaces, for example, the computational mesh can remain completely structured. If the underlying problem has some special structure dividing the computational domain in subdomains, for instance, defined by grains with a specific permeability or microstructure, the domain boundaries are allowed to cut through the background mesh in a close to arbitrary fashion. By including boundary or interface defining terms in the variational formulation the method essentially eliminates the meshing problem. This is particularly convenient in shape optimization problems [27, Chapter 6] or inverse identification problems [5], where the position of the interfaces changes during an optimization process. The introduction of a skeletal variable makes it possible to eliminate internal degrees of freedom in a parallel fashion so that the linear system can be solved by iterating on the Schur complement. Optimal stability and accuracy is obtained using the tools developed within the CutFEM paradigm. Below we will also show that the resulting Schur complement has a condition number that is bounded independently of the mesh interface intersection.

Brief review of cut finite elements.   CutFEMs were originally introduced by Hansbo and Hansbo [23] as an alternative to extended finite element methods, using Nitsche's method as mortaring over an unfitted interface. The ideas were extended to composite meshes, Chimera-style, by Hansbo, Hansbo and Larson [24] and then to fictitious domain problems by Burman and Hansbo [7]. In a parallel development [36], Olshanskii, Reusken, and Grande developed a CutFEM for the discretization of PDEs on surfaces using the trace of the (discrete) surface on a finite element bulk mesh as the computational mesh. Additional stability can be obtained by adding suitable stabilization terms [3, 8, 12, 31, 22] and the methods are then comparable to standard finite element methods on meshed geometries, with respect to both conditioning and accuracy. Further developments include techniques for the handling of curved interfaces or boundaries [32, 9], PDEs on composite surfaces [25], and transport problems in fractured mixed dimensional domains [11]. For an overview of the ideas behind the CutFEM paradigm see [4], and for a collection of essays giving a snapshot of the state of the art we refer to [2].

New contributions. We develop a hybridized CutFEM for an elliptic model problem with piecewise constant coefficients defined on a partition of the domain. The union of the boundaries of the subdomains is called the skeleton and hybridization consists of adding a solution field representing the solution on the skeleton. In the proposed method each subdomain of the bulk and each component of the skeleton is equipped with its own finite element mesh and space. The mesh may be constructed using a cut technique or a standard mesh. The hybridization leads to a convenient formulation which also naturally facilitates elimination of the bulk degrees of freedom using a Schur complement formulation.

We develop a stability and error analysis where we in particular show that optimal order a priori error estimates hold for both and that the condition number of the Schur complement is $O(d^{-1}h^{-1})$, where d is the diameter of the subdomain. We cover very general choices of the subdomains and one instance of our method and analysis is a p based discontinuous Galerkin method on polygonal elements.

Earlier work. Hybridized methods are commonly used and many versions have been proposed, notably in the setting of discontinuous Galerkin methods; for an overview, see Cockburn, Gopalakrishnan, and Lazarov [16]. The particular version we employ here was first proposed using meshed subdomains by Egger [18], who later extended it to incompressible flow [20, 21] and convection-diffusion problems [19]; cf. also Könnö and Stenberg [30], where it was employed for solving the Brinkman problem. Independently, the same approach has been proposed by Oikawa and Kikuchi [35] and further developed by Miyashita and Saito [34].

Outline. In section 2 we formulate the hybridized CutFEM. In section 3 we derive stability and optimal order error estimates. In section 4 we eliminate the bulk fields using the Schur complement and we derive a bound for the condition number of the Schur complement. In section 5 we present numerical results.

2. The hybridzed cut finite element method.

2.1. The model problem.

Domain. In hybridized methods the domain Ω is partitioned into a set of subdomains $\{\Omega_i\}_{i=1}^N$ and the interfaces between the subdomains constitute a skeleton Ω_0; see the illustration in Figure 1. Formally we assume the following:

- Let $\Omega \subset \mathbb{R}^d$, with $d = 2$ or 3, be a domain with piecewise smooth Lipschitz boundary $\partial\Omega$. Recall that $\partial\Omega$ is piecewise smooth if it is the union of a finite number of smooth $d-1$ dimensional manifolds with boundary and Lipschitz if there is a finite set of local coordinate systems in which the boundary can be described as a Lipschitz function.

- Let $\{\Omega_i\}_{i=1}^N$ be a partition of Ω into N subdomains Ω_i with piecewise smooth Lipschitz boundaries $\partial\Omega_i$. For the analysis we assume that this partition is such that the following trace inequality holds for each subdomain:

$$(2.1) \qquad \|v\|_{\partial\Omega_i}^2 \leq C\left(d_{\Omega_i}^{-1}\|v_i\|_{\Omega_i}^2 + d_{\Omega_i}\|\nabla v_i\|_{\Omega_i}^2\right),$$

  where $d_{\Omega_i} = \operatorname{diam}(\Omega_i)$.

- Let $\Omega_0 = \cup_{i=1}^N \partial\Omega_i \setminus \partial\Omega$ be the skeleton of the partition. Note that there is a partition of Ω_0 into smooth $d-1$ manifolds with boundary

$$(2.2) \qquad \Omega_0 = \cup_{i,j=1}^N \partial\Omega_i \cap \partial\Omega_j = \cup_{k=1}^{N_0} \Omega_{0,k},$$

  where N_0 is the number of nonempty intersections $\partial\Omega_i \cap \partial\Omega_j$. We denote $\Omega_{0,k}$ a skeleton subdomain and for increased readability we from here on reserve the index $k = 1, \ldots, N_0$ for identifying skeleton subdomains, whereas indices $i, j = 0, \ldots, N$ are used to identify subdomains Ω_i, Ω_j.
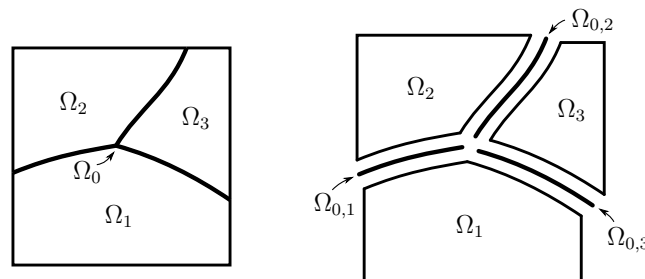

FIG. 1. *Schematic illustration of a partition of the domain Ω into a set of subdomains $\{\Omega_i\}_{i=1}^N$ and of the skeleton Ω_0 with its partition into a set of skeleton subdomains $\{\Omega_{0,k}\}_{k=1}^{N_0}$.*

Model problem. We consider the following hybridized formulation of the Poisson problem: find $u_0 : \Omega_0 \to \mathbb{R}$ and for $i = 1, \ldots, N$, $u_i : \Omega_i \to \mathbb{R}$ such that

$$
\begin{align}
-\nabla \cdot a_i \nabla u_i &= f_i & &\text{in } \Omega_i, \tag{2.3}\\
[\![n \cdot a \nabla u]\!] &= 0 & &\text{on } \Omega_0, \tag{2.4}\\
[u]_i &= 0 & &\text{on } \partial\Omega_i \cap \Omega_0, \tag{2.5}\\
u_i &= 0 & &\text{on } \partial\Omega_i \cap \partial\Omega. \tag{2.6}
\end{align}
$$

Here a_i, $i = 1, \ldots, N$, are positive constants and the jumps operators are defined by

$$
[u]|_{\partial\Omega_i \cap \Omega_0} = u_i - u_0, \qquad [\![n \cdot a \nabla u]\!]|_{\partial\Omega_i \cap \partial\Omega_j} = n_i \cdot a_i \nabla u_i + n_j \cdot a_j \nabla u_j, \tag{2.7}
$$

where n_i is the exterior unit normal to Ω_i.

This problem is well posed, with exact solution $u \in H_0^1(\Omega)$ such that $u_i = u|_{\Omega_i}$, $i = 0, \ldots, N$. Below we will assume the additional regularity $u_i \in H^{\frac{3}{2}}(\Omega_i)$. We define the spaces

$$
V_0 = \bigoplus_{k=1}^{N_0} H^1(\Omega_{0,k}), \quad V_{1,N} = \bigoplus_{i=1}^{N} H^{\frac{3}{2}}(\Omega_i) \tag{2.8}
$$

and the global space

$$
W = V_0 \oplus V_{1,N}. \tag{2.9}
$$

We will use the notation $(\cdot, \cdot)_X$ for the L^2-scalar product over $X \subset \mathbb{R}^s$, where either $s = d$ or $s = d - 1$. The associated norm will be denoted $\| \cdot \|_X$. We will also use the following weighted L^2 norm, $\|v\|_{\omega,a}^2 = (av, v)_\omega$, for $a \in L^\infty(\omega)$ with $a > 0$.

Remark 2.1. We note that solutions to certain problems of the form (2.3)–(2.6) may have regularity arbitrarily close to $H^1(\Omega)$; see [29], where a problem with intersecting interfaces and discontinuous coefficients is considered. Thus $u_i \in H^{\frac{3}{2}}(\Omega_i)$ does not hold in general. For smooth interfaces the assumption holds and, of course, for the situation when the coefficient is globally constant. Both of these cases are of practical importance since hybridization is used to conveniently enable elimination of the subdomain unknowns using a Schur complement procedure; see section 3. Deriving error bounds with lower regularity assumptions requires a more involved analysis and we refer to the techniques developed in [10] for CutFEM approximations of boundary value problems with mixed Dirichlet/Neumann boundary conditions and minimal regularity requirements.

2.2. The method.

Finite element spaces. On each subdomain Ω_i, $1 \le i \le N$, and on each skeleton subdomain $\Omega_{0,k}$, $1 \le k \le N_0$, we construct a separate finite element space.

- Let $O \in \{\Omega_{0,k}\}_{k=1}^{N_0} \cup \{\Omega_i\}_{i=1}^{N}$, i.e., O is either one of the d dimensional bulk subdomains Ω_i or one of the $d-1$ dimensional components of the skeleton Ω_0.
- For each O there is a d dimensional domain U_O such that $O \subseteq U_O$. For each $h \in (0, h_{\max,O}]$, where $h_{\max,O} > 0$ is a sufficiently small parameter, there is a d dimensional quasiuniform mesh $\mathcal{T}_h(U_O)$ on U_O with mesh parameter h, i.e., $\mathcal{T}_h(U_O)$ is a partition of U_O into shape regular elements T with diameter h_T and $h_T \sim h$ uniformly. The active mesh is defined by

$$
\mathcal{T}_{h,O} = \{T \in \mathcal{T}_h(U_O) : T \cap O \ne \emptyset\}, \tag{2.10}
$$

(a) U_{Ω_i} (b) $\mathcal{T}_h(U_{\Omega_i})$ (c) $\mathcal{T}_{h,\Omega_i} = \mathcal{T}_{h,i}$

(d) $U_{\Omega_{0,k}}$ (e) $\mathcal{T}_h(U_{\Omega_{0,k}})$ (f) $\mathcal{T}_{h,\Omega_{0,k}} = \mathcal{T}_{h,0,k}$
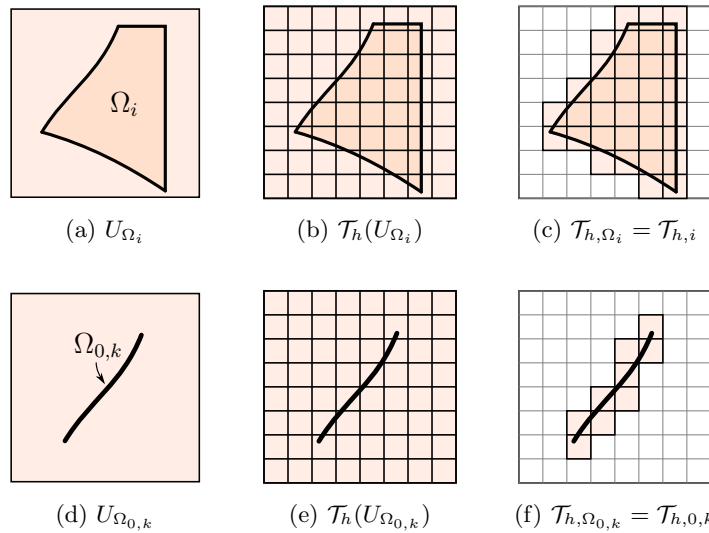
FIG. 2. *Illustration of the subdomainwise construction of meshes. Note that there is no requirement for the meshes to match.* (a)–(c) *Construction on a subdomain Ω_i.* (d)–(f) *Construction on a skeleton subdomain $\Omega_{0,k}$.*

which covers O but is not required to perfectly match O. This construction of the active mesh is illustrated in Figure 2.

• Let $V_{h,O}$ be a finite dimensional space consisting of continuous piecewise polynomial functions defined on $\mathcal{T}_{h,O}$ such that there is an interpolation operator $\pi_h : H^1(\mathcal{T}_{h,O}) \to V_{h,O}$, which satisfy the approximation property

$$(2.11) \qquad \|v - \pi_h v\|_{H^m(\mathcal{T}_{h,O})} \lesssim h^{s-m} \|v\|_{H^s(\mathcal{T}_{h,O})}, \qquad 0 \le m \le s \le p+1,$$

where $p+1$ is the approximation order of $V_{h,O}$. We employ the notation $a \lesssim b \Leftrightarrow a \le Cb$, with analogous notation for greater or equal $\gtrsim$ and equivalence $\sim$. The hidden constants in this notation are always independent of the mesh size.

• For $O \in \{\Omega_i\}_{i=1}^N$ we use the simplified notation

$$(2.12) \qquad\qquad V_{h,i} = V_{h,\Omega_i}, \qquad \mathcal{T}_{h,i} = \mathcal{T}_{h,\Omega_i},$$

and for $O \in \{\Omega_{0,k}\}_{k=1}^{N_0}$,

$$(2.13) \qquad V_{h,0,k} = V_{h,\Omega_{0,k}}, \qquad \mathcal{T}_{h,0,k} = \mathcal{T}_{h,\Omega_{0,k}}, \qquad \mathcal{T}_{h,0} = \sqcup_{k=1}^{N_0} \mathcal{T}_{h,0,k}.$$

• Define the finite element spaces

$$(2.14) \qquad\qquad V_{h,0} = \bigoplus_{k=1}^{N_0} V_{h,0,k}, \qquad V_{h,1,N} = \bigoplus_{i=1}^N V_{h,i}$$

and

$$(2.15) \qquad\qquad\qquad W_h = V_{h,0} \oplus V_{h,1,N}.$$

Remark 2.2. Here we are using restrictions of d dimensional spaces to the $d-1$ dimensional skeleton in the spirit of CutFEM (see [8, 36]), where similar ideas are used to solve the Laplace–Beltrami problem on a codimension one surface embedded in d dimensional mesh. We may also use a standard $d-1$ dimensional mesh on each of the components $\Omega_{0,i}$ of the skeleton. Note that these meshes do not need to match on the interfaces $\overline{\Omega}_{0,i} \cap \overline{\Omega}_{0,j}$ between two components of the skeleton. Our analysis readily extends to this situation as well.

Stabilization forms. We here define a number of abstract properties, which we assume our stabilization forms satisfy. In section 3.3 below we construct forms that fulfill these properties. On each subdomain Ω_i, $1 \leq i \leq N$, there is a symmetric bilinear form $s_{h,i}$, on $V_{h,i} + H^{p+1}(\Omega_i)$, with associated seminorm $\| \cdot \|_{s_{h,i}}$ such that

- we have consistency and interpolation estimates,

$$(2.16) \qquad \|v\|_{s_{h,i}} \lesssim h^{s-1}|v|_{H^s(\Omega_i)},$$

$$(2.17) \qquad \|v - \pi_h v\|_{s_{h,i}} \lesssim h^{s-1}|v|_{H^s(\Omega_i)},$$

where $1 \leq s \leq p+1$;

- we have inverse estimates,

$$(2.18) \qquad h\|\nabla v\|_{\partial\Omega_i,a_i}^2 \lesssim \|\nabla v\|_{\Omega_i,a_i}^2 + \|v\|_{s_{h,i}}^2, \qquad v \in V_{h,i},$$

$$(2.19) \qquad \|v\|_{\mathcal{T}_{h,i}}^2 \lesssim \|v\|_{\Omega_i}^2 + \|v\|_{s_{h,i}}^2, \qquad v \in V_{h,i}.$$

On each skeleton subdomain $\Omega_{0,k}$, $1 \leq k \leq N_0$, there is a symmetric bilinear form $s_{h,0,k}$, on $V_{h,0,k} + H^{p+1/2}(\Omega_{0,k})$, with associated seminorm $\| \cdot \|_{s_{h,0,k}}$ such that

- we have consistency and interpolation estimates,

$$(2.20) \qquad \|v\|_{s_{h,0,k}} \lesssim h^{s-1}|v|_{H^{s-1/2}(\Omega_{0,k})},$$

$$(2.21) \qquad \|v - \pi_h v\|_{s_{h,0,k}} \lesssim h^{s-1}|v|_{H^{s-1/2}(\Omega_{0,k})},$$

where $1 \leq s \leq p+1$;

- we have the inverse estimate

$$(2.22) \qquad h^{-1}\|v\|_{\mathcal{T}_{h,0,k}}^2 \sim \|v\|_{\Omega_{0,k}}^2 + \|v\|_{s_{h,0,k}}^2, \qquad v \in V_{h,0,k}.$$

For notational convenience we define the skeleton stabilization form, respectively, the total stabilization form,

$$(2.23) \qquad s_{h,0}(v_0, w_0) = \sum_{k=1}^{N_0} s_{h,0,k}(v_{0,k}, w_{0,k}), \qquad s_h(v, w) = \sum_{i=0}^{N} s_{h,i}(v_i, w_i),$$

with their respective associated seminorms $\| \cdot \|_{s_{h,0}}$ and $\| \cdot \|_{s_h}$.

Derivation of the method. Multiplying (2.3) by a test function v, integrating by parts over Ω_i, and using the convention $u_0 = 0$ on $\partial\Omega$ we obtain

$$(2.24) \qquad \sum_{i=1}^{N} (f_i, v_i)_\Omega = \sum_{i=1}^{N} -(\nabla \cdot a_i \nabla u_i, v_i)_{\Omega_i}$$

$$(2.25) \qquad = \sum_{i=1}^{N} (a_i \nabla u_i, \nabla v_i)_{\Omega_i} - (n_i \cdot a_i \nabla u_i, v_i)_{\partial\Omega_i}$$

$$(2.26) \qquad = \sum_{i=1}^{N} (a_i \nabla u_i, \nabla v_i)_{\Omega_i} - (n_i \cdot a_i \nabla u_i, v_i)_{\partial\Omega_i}$$

$$(2.27) \qquad - (u_i - u_0, n \cdot a_i \nabla v_i)_{\partial\Omega_i} + (\beta h^{-1} a_i(u_i - u_0), v_i)_{\partial\Omega_i}$$

$$(2.28) \qquad = \sum_{i=1}^{N} (a_i \nabla u_i, \nabla v_i)_{\Omega_i} + s_{h,i}(u_i, v_i) - (n_i \cdot a_i \nabla u_i, v_i - v_0)_{\partial\Omega_i}$$

$$(2.29) \qquad - (u_i - u_0, n_i \cdot a_i \nabla v_i)_{\partial\Omega_i} + (\beta h^{-1} a_i(u_i - u_0), (v_i - v_0))_{\partial\Omega_i},$$

where we added terms which are zero for the exact solution u with the purpose of obtaining a stable symmetric formulation. More precisely, in (2.27) we used (2.5) to add terms involving $[u]_i = u_i - u_0 = 0$ and in (2.28) we used (2.4) and the identity

$$(2.30) \qquad 0 = (\llbracket n \cdot a \nabla u \rrbracket, v_0)_{\Omega_0} = \sum_{i=1}^{N} (n_i \cdot a_i \nabla u_i, v_0)_{\partial\Omega_i}$$

since $v_0 = 0$ on $\partial\Omega$. Finally, we added the stabilization form $s_{h,i}$ using consistency (2.16).

Definition of the method. Find $u_h \in W_h$ such that

$$(2.31) \qquad A_h(u_h, v) = l_h(v) \qquad \forall v \in W_h,$$

where W_h is defined in (2.15) and

$$(2.32) \qquad A_h(v, w) = s_{h,0}(v_0, w_0)$$

$$(2.33) \qquad + \sum_{i=1}^{N} \Big((a_i \nabla v_i, \nabla w_i)_{\Omega_i} + s_{h,i}(v_i, w_i) + (\beta h_i^{-1} a_i[v]_i, [w]_i)_{\partial\Omega_i}$$

$$(2.34) \qquad - (n_i \cdot a_i \nabla v_i, [w]_i)_{\partial\Omega_i} - ([v]_i, n_i \cdot a_i \nabla w_i)_{\partial\Omega_i} \Big)$$

$$(2.35) \qquad l_h(v) = \sum_{i=1}^{N} (f_i, v_i)_{\Omega_i}.$$

Remark 2.3. We consider the partition $\{\Omega_i\}_{i=1}^{N}$ of Ω as being fixed for simplicity only. In fact we may also allow the number of subdomains N to increase during refinement. We then obtain a version of the polygonal finite element method, where each polygonal finite element is equipped with a mesh and piecewise continuous polynomials of degree p, and not only polynomials of order p which in general is the case in polygonal finite elements. In order to guarantee that coercivity holds under refinement of the partition we essentially need the inverse inequality (2.18) to hold with a uniform constant for all subdomains that occur during the refinement of the partition. Therefore we need to assume some additional shape regularity of the subdomains. For instance, we may assume that for each Ω_i there is partition $\mathcal{S}_i$ of Ω_i into simplicies S and a constant such that for all $S \in \mathcal{S}_i$ with $|\partial S \cap \partial\Omega| > 0$ it holds that

$$(2.36) \qquad h_i \lesssim \frac{|S|}{|\partial S \cap \partial\Omega_i|},$$

where the mesh parameter $h_i \in (0, h_{0,\Omega_i}]$. Then (2.18) holds uniformly over all partitions $\{\Omega_i\}_{i=1}^{N}$ of Ω, with corresponding meshes $\mathcal{T}_{h,i}$.

The corresponding condition for polygonal finite elements is

$$(2.37) \qquad \mathrm{diam}(\Omega_i) \lesssim \frac{|S|}{|\partial S \cap \partial\Omega_i|}$$

(see Assumption 30, section 4.3 in [13]), and since we may always assume that $h_i \lesssim \mathrm{diam}(\Omega_i)$ we conclude that (2.36) is weaker than (2.37) and thus more complex subdomains may be employed when finer meshes are used.

Weak Galerkin orthogonality. Let $u \in W$ be the solution to (2.3)–(2.6) and $u_h \in W_h$ be the solution to (2.31). The following weak Galerkin orthogonality holds:

$$A_h(u - u_h, v) = s_h(u, v) \qquad \forall v \in W_h,$$
(2.38)

where the right-hand side is nonzero since the stabilization forms are not consistent.

3. Error estimates. The error estimates for our methods are obtained in a similar fashion as those proven in [18] and we will focus here on how robustness and optimal estimates are obtained in the framework of cut elements.

3.1. Properties of A_h. Define the energy norm

$$\||v\||_h^2 = \|v_0\|_{s_{h,0}}^2 + \sum_{i=1}^{N} \|\nabla v_i\|_{\Omega_i, a_i}^2 + h\|\nabla v_i\|_{\partial\Omega_i, a_i}^2 + h^{-1}\|[v]_i\|_{\partial\Omega_i, a_i}^2 + \|v_i\|_{s_{h,i}}^2.$$
(3.1)

LEMMA 3.1 (continuity and coercivity). *There exist positive constants such that A_h is continuous,*

$$A_h(v, w) \lesssim \||v\||_h \||w\||_h, \qquad v, w \in W + W_h,$$
(3.2)

and for β large enough A_h is coercive

$$\||v\||_h^2 \lesssim A_h(v, v), \qquad v \in W_h.$$
(3.3)

Proof. Continuity (3.2). This follows directly from the Cauchy–Schwarz inequality.
Coercivity (3.3). Using standard arguments and the inverse estimate (2.18) we obtain

$$(3.4) \quad A_h(v, v) = s_{h,0}(v_0, v_0) + \sum_{i=1}^{N} (a_i \nabla v_i, \nabla v_i)_{\Omega_i} + s_{h,i}(v_i, v_i) + \beta h^{-1}\|[v]_i\|_{\partial\Omega_i, a_i}^2$$

$$(3.5) \qquad\qquad - 2(n_i \cdot a_i \nabla v_i, [v_i])_{\partial\Omega_i}$$

$$(3.6) \qquad \gtrsim \|v_0\|_{s_{h,0}}^2 + \sum_{i=1}^{N} \|\nabla v_i\|_{\Omega_i, a_i}^2 + \|v\|_{s_{h,i}}^2 + \beta h^{-1}\|[v]_i\|_{\partial\Omega_i, a_i}^2$$

$$(3.7) \qquad\qquad - 2h^{1/2}\|\nabla v_i\|_{\partial\Omega_i, a_i} h^{-1/2}\|[v_i]\|_{\partial\Omega_i, a_i}$$

$$(3.8) \qquad \gtrsim \|v_0\|_{s_{h,0}}^2 + \sum_{i=1}^{N} \left(\|\nabla v_i\|_{\Omega_i, a_i}^2 + \|v\|_{s_{h,i}}^2 - \delta h\|\nabla v_i\|_{\partial\Omega_i, a_i}^2 \right)$$

$$(3.9) \qquad\qquad + (\beta - \delta^{-1})h^{-1}\|[v]_i\|_{\partial\Omega_i, a_i}^2$$

$$(3.10) \qquad \gtrsim \|v_0\|_{s_{h,0}}^2 + \sum_{i=1}^{N} (1 - \delta C_1) \left(\|\nabla v_i\|_{\Omega_i, a_i}^2 + \|v\|_{s_{h,i}}^2 \right)$$

$$(3.11) \qquad\qquad + (\beta - \delta^{-1})h^{-1}\|[v]_i\|_{\partial\Omega_i, a_i}^2,$$

where C_1 is the hidden constant in (2.18). Coercivity thereby holds if $0 < \delta < C_1^{-1}$ and $\beta > \delta^{-1}$. $\qquad\qquad\square$

LEMMA 3.2 (Poincaré inequality). *Let ϕ be the solution to the dual problem*

$$-\nabla \cdot a\nabla\phi = \psi \text{ in } \Omega \qquad \phi = 0 \text{ on } \partial\Omega$$
(3.12)

with $\psi \in L^2(\Omega)$, and assume that

$$(3.13) \qquad \sum_{i=1}^{N} \|\phi_i\|_{H^{3/2}(\Omega_i),a_i}^2 \lesssim \|\psi\|_{\Omega}^2.$$

Under the regularity assumption (3.13) the following Poincaré estimate holds:

$$(3.14) \qquad \Big(\min_{1 \le i \le N} d_{\Omega_i}\Big) h^{-1} \|v_0\|_{\mathcal{T}_{h,0}}^2 + \sum_{i=1}^{N} \|v_i\|_{\mathcal{T}_{h,i}}^2 \lesssim \||v\||_h^2, \qquad v \in W_h,$$

where d_{Ω_i} is the diameter of Ω_i. This estimate in particular shows that $\|| \cdot \||_h$ is a norm on W_h.

Proof. Considering first the estimation of the bulk subdomain contributions, we note that using (2.19) we have

$$(3.15) \qquad \sum_{i=1}^{N} \|v\|_{\mathcal{T}_{h,i}}^2 \lesssim \sum_{i=1}^{N} \|v\|_{\Omega_i}^2 + \|v\|_{s_{h,i}}^2.$$

To estimate the term $\sum_{i=1}^{N} \|v\|_{\Omega_i}^2$ we multiply the dual problem (3.12) by $v \in W_h$, and using partial integration on each Ω_i we obtain

$$(3.16) \quad \sum_{i=1}^{N} (v_i, \psi_i)_{\Omega_i} = \sum_{i=1}^{N} (a_i \nabla v_i, \nabla \phi_i)_{\Omega_i} - (v_i, n_i \cdot a_i \nabla \phi_i)_{\partial\Omega_i}$$

$$(3.17) \qquad = \sum_{i=1}^{N} (a_i \nabla v_i, \nabla \phi_i)_{\Omega_i} - ([v]_i, n_i \cdot a_i \nabla \phi_i)_{\partial\Omega_i} - (v_0, n_i \cdot a_i \nabla \phi_i)_{\partial\Omega_i}$$

$$(3.18) \qquad = \sum_{i=1}^{N} (a_i \nabla v_i, \nabla \phi_i)_{\Omega_i} - ([v]_i, n_i \cdot a_i \nabla \phi_i)_{\partial\Omega_i} - (v_0, \underbrace{[\![n \cdot a\nabla\phi]\!]}_{=0})_{\Omega_0}$$

$$(3.19) \qquad \lesssim \sum_{i=1}^{N} \|\nabla v_i\|_{\Omega_i,a_i} \|\nabla \phi_i\|_{\Omega_i,a_i} + h^{-1/2}\|[v]_i\|_{\partial\Omega_i,a_i} h^{1/2}\|\nabla \phi_i\|_{\partial\Omega_i,a_i}$$

$$(3.20) \qquad \lesssim \||v\||_h \underbrace{\Big(\sum_{i=1}^{N} \|\nabla \phi\|_{\Omega_i,a_i}^2 + h\|\phi\|_{H^{3/2}(\Omega_i),a_i}^2\Big)^{1/2}}_{\lesssim \|\psi\|_{\Omega}}$$

$$(3.21) \qquad \lesssim \||v\||_h \|\psi\|_{\Omega},$$

where in (3.17) we added and subtracted v_0 in the boundary terms; in (3.18) we used the fact that $v_0 = 0$ on $\partial\Omega$; in (3.19) we used the Cauchy–Schwarz inequality and the fact that $[\![n \cdot a\nabla\phi]\!] = 0$ on Ω_0; in (3.20) we used the definition (3.1) of the energy norm and a trace inequality for ϕ; and finally in (3.21) we used the regularity assumption (3.13). Thus we obtain

$$(3.22) \qquad \sum_{i=1}^{N} \|v_i\|_{\mathcal{T}_{h,i}}^2 \lesssim \||v\||_h^2.$$

Next using the trace inequality (2.1)

$$(3.23) \qquad \|v\|_{\partial\Omega_i}^2 \lesssim d_{\Omega_i}^{-1}\|v_i\|_{\Omega_i}^2 + d_{\Omega_i}\|\nabla v_i\|_{\Omega_i}^2$$

$$(3.24) \qquad\qquad \le d_{\Omega_i}^{-1}\|v_i\|_{\Omega_i}^2 + d_{\Omega_i}\|a_i^{-1}\|_{L^\infty(\Omega_i)}\|\nabla v_i\|_{\Omega_i,a_i}^2$$

we have that

$$(3.25) \qquad \|v_0\|_{\Omega_0}^2 \lesssim \sum_{i=1}^N \|[v]_i\|_{\partial\Omega_i}^2 + \|v_i\|_{\partial\Omega_i}^2$$

$$(3.26) \qquad\qquad \lesssim \sum_{i=1}^N \|[v]_i\|_{\partial\Omega_i}^2 + d_{\Omega_i}^{-1}\|v_i\|_{\Omega_i}^2 + d_{\Omega_i}\|a_i^{-1}\|_{L^\infty(\Omega_i)}\|\nabla v_i\|_{\Omega_i,a_i}^2$$

$$(3.27) \qquad\qquad \lesssim \Big(\min_{1\le i\le N} d_{\Omega_i}\Big)^{-1}\|\|v\|\|_h^2,$$

where we in the last inequality assume that diameter of each bulk subdomain $d_{\Omega_i} \le \text{diam}(\Omega) \sim 1$ is small enough for

$$(3.28) \qquad \max_{1\le i\le N} d_{\Omega_i}^{-1} \ge \max_{1\le i\le N} d_{\Omega_i}\|a_i^{-1}\|_{L^\infty(\Omega_i)}.$$

Thus by (2.22) we obtain

$$(3.29) \qquad h^{-1}\|v_0\|_{\mathcal{T}_{h,0}}^2 \lesssim \|v_0\|_{\Omega_0}^2 + \|v_0\|_{s_{h,0}}^2 \lesssim \Big(1 + \Big(\min_{1\le i\le N} d_{\Omega_i}\Big)^{-1}\Big)\|\|v\|\|_h^2,$$

which concludes the proof since $1 \lesssim \big(\min_{1\le i\le N} d_{\Omega_i}\big)^{-1}$. $\qquad\qquad\square$

Note in particular that we have the estimate

$$(3.30) \qquad \Big(\min_{1\le i\le N} d_{\Omega_i}\Big)h^{-1}\|v_0\|_{\mathcal{T}_{h,0}}^2 \lesssim \|\|v_0 + w\|\|_h^2$$

for all $w \in V_{h,1,N} = \oplus_{i=1}^N V_{h,i}$.

3.2. Interpolation operator.

Definition of the interpolation operator. In order to handle both the d dimensional components and the $d-1$ dimensional components at the same time we let $O \in \{\Omega_{0,k}\}_{k=1}^{N_0} \cup \{\Omega_i\}_{i=1}^N$, i.e., O is either one of the d dimensional bulk domains Ω_i or one of the $d-1$ dimensional components of the skeleton Ω_0.

- There is an extension operator $E_O : H^s(O) \to H^s(U_\delta(O))$ such that

$$(3.31) \qquad \|E_O v\|_{H^s(U_\delta(O))} \lesssim \begin{cases} \delta^{1/2}\|v\|_{H^s(O)}, & \dim(O) = d-1, \\ \|v\|_{H^s(O)}, & \dim(O) = d, \end{cases}$$

  where $U_\delta(O) = \cup_{x\in O} B_\delta(x)$, with $B_\delta(x)$ denoting a d dimensional ball with radius $\delta > 0$ centered in x. Thus, $U_\delta(O)$ is always a d dimensional tubular neighborhood of O even if O itself is $d-1$ dimensional. The $d-1$ dimensional case of (3.31) includes the parameter $0 < \delta < \delta_0$ which for h small enough we may take as $\delta \sim h$; see [37, Lemma 3.1]. In proofs below we will utilize that the construction of the extension operator on a skeleton subdomain $\Omega_{0,k}$ is such that the function is first extended onto a smooth continuation of $\Omega_{0,k}$, whereafter this extended function is in turn extended onto $U_\delta(\Omega_{0,k})$ via the closest point mapping. The extended function on a skeleton subdomain is thus constant in the normal direction.

- Let $\pi_{h,O,SZ} : H^{1/2+\epsilon}(\mathcal{T}_{h,O}) \to V_{h,O}$ be a Scott–Zhang interpolant, without special treatment of the boundary condition, for which the standard interpolation estimate

$$(3.32) \qquad \|v - \pi_{h,O,SZ}v\|_{H^m(\mathcal{T}_{h,O})} \lesssim h^{s-m}\|v\|_{H^s(\mathcal{T}_{h,O})}$$

holds for $0 \le m \le s \le p+1$; see [38]. Recall that the Scott–Zhang interpolant is a projection such that $\pi_{h,O,SZ}(\pi_{h,O,SZ}v) = \pi_{h,O,SZ}v$. Using the extension operator we define $\pi_{h,O} : H^s(O) \to V_{h,O}$ as

$$(3.33) \qquad \pi_{h,O}v = \pi_{h,O,SZ}E_O v,$$

and finally, we let $\pi_h : (\oplus_{k=1}^{N_0} H^{s-1/2}(\Omega_{0,k})) \oplus (\oplus_{i=1}^{N} H^s(\Omega_i)) \to W_h$ be defined componentwise by $(\pi_h v)_O = \pi_{h,O}v|_O$. We then have the interpolation error estimate

$$(3.34) \qquad \|v - \pi_h v\|_{H^m(O)} \lesssim h^{s-m}\|v\|_{H^s(O)}$$

for $0 \le m \le s \le p + 1$. For the d dimensional subdomains $O = \Omega_i$, $i = 1, \ldots, N$, we derive (3.34) using a standard interpolation error bound for the Scott–Zhang interpolant followed by the stability of the extension operator

$$(3.35) \qquad \|(I - \pi_h)v\|_{H^m(\Omega_i)} \le \|(I - \pi_h)E_{\Omega_i}v\|_{H^m(\mathcal{T}_{h,i})}$$
$$(3.36) \qquad\qquad\qquad \lesssim h^{s-m}\|E_{\Omega_i}v\|_{H^s(\mathcal{T}_{h,i})} \lesssim h^{s-m}\|v\|_{H^s(\Omega_i)}.$$

For the $d-1$ dimensional skeleton subdomains $\Omega_{0,k}$, $k = 1, \ldots, N_0$, we instead employ the trace inequality

$$(3.37) \qquad \|v\|_{\Omega_{0,k}}^2 \lesssim h^{-1}\|v\|_{\mathcal{T}_{h,0,k}}^2 + h\|\nabla v\|_{\mathcal{T}_{h,0,k}}^2$$

whereafter (3.34) can be derived in the same way as in (3.35)–(3.36).

LEMMA 3.3 (interpolation error estimate). *The following estimate holds:*

$$(3.38) \qquad \||v - \pi_h v\||_h^2 \lesssim h^{2p} \left(\sum_{k=1}^{N_0} \|v_{0,k}\|_{H^{p+1/2}(\Omega_{0,k})}^2 + \sum_{i=1}^{N} \|v_i\|_{H^{p+1}(\Omega_i)}^2 \right).$$

Remark 3.4. Note that here we can easily localize h and p to the subdomains and skeleton subdomains, but for notational clarity we keep a global mesh parameter h and order of polynomials p.

Proof of (3.38). Let $\eta = v - \pi_h v$ be the interpolation error and using the definition (3.1) of the energy norm we have

(3.39)

$$\||\eta\||_h^2 = \|\eta_0\|_{s_{h,0}}^2 + \underbrace{\sum_{i=1}^{N} \|\nabla\eta_i\|_{\Omega_i,a_i}^2 + h\|\nabla\eta_i\|_{\partial\Omega_i,a_i}^2 + h^{-1}\|[\eta]_i\|_{\partial\Omega_i,a_i}^2}_{=\bigstar} + \|\eta_i\|_{s_{h,i}}^2,$$

where the first and last terms are handled using the interpolation properties (2.21) and (2.17) of the stabilization forms. For the remaining terms we proceed as

$$(3.40) \qquad \bigstar \lesssim \sum_{i=1}^{N} \|\nabla \eta_i\|_{\Omega_i}^2 + h\|\nabla \eta\|_{\partial \Omega_i}^2 + h^{-1}\|\eta_i\|_{\partial \Omega_i}^2 + h^{-1}\|\eta_0\|_{\partial \Omega_i}^2$$

$$(3.41) \qquad \lesssim \sum_{i=1}^{N} \|\nabla \eta_i\|_{\Omega_i}^2 + h\|\nabla \eta_i\|_{\partial \Omega_i}^2 + h^{-1}\|\eta_i\|_{\partial \Omega_i}^2 + \sum_{k=1}^{N_0} h^{-1}\|\eta_{0,k}\|_{\Omega_{k,0}}^2$$

$$(3.42) \qquad \lesssim \sum_{i=1}^{N} \|\nabla \eta_i\|_{\Omega_i}^2 + \left(\|\nabla \eta_i\|_{\mathcal{T}_{h,i}(\partial \Omega_i)}^2 + h^2\|\nabla^2 \eta_i\|_{\mathcal{T}_{h,i}(\partial \Omega_i)}^2\right)$$

$$(3.43) \qquad + \left(h^{-2}\|\eta_i\|_{\mathcal{T}_{h,i}(\partial \Omega_i)}^2 + \|\nabla \eta_i\|_{\mathcal{T}_{h,i}(\partial \Omega_i)}^2\right) + \sum_{k=1}^{N_0} h^{-1}\|\eta_{0,k}\|_{\Omega_{k,0}}^2$$

$$(3.44) \qquad \lesssim \sum_{i=1}^{N} h^{2p}\|v_i\|_{H^{p+1}(\Omega_i)}^2 + \sum_{k=1}^{N_0} h^{2p}\|v_{0,k}\|_{H^{p+1/2}(\Omega_{0,k})}^2,$$

where we in (3.40) use lower bounds on the coefficients a_i and the Cauchy–Schwarz inequality; in (3.41) we separate the skeleton terms; in (3.42)–(3.43) we employ the trace inequality

$$(3.45) \qquad \|v\|_{\partial \Omega_i}^2 \lesssim h^{-1}\|v\|_{\mathcal{T}_{h,i}(\partial \Omega_i)}^2 + h\|\nabla v\|_{\mathcal{T}_{h,i}(\partial \Omega_i)}^2,$$

where $\mathcal{T}_{h,i}(\partial \Omega_i)$ is the set of all elements in $\mathcal{T}_{h,i}$ which intersect $\partial \Omega_i$; and finally, in (3.44) we employ the interpolation estimates (3.32) and (3.34). $\qquad \square$

3.3. Stabilization forms. Define the following stabilization forms:
- For each subdomain Ω_i, $1 \leq i \leq N$, define the stabilization form

$$(3.46) \qquad s_{h,i}(v,w) = \sum_{\ell=1}^{p} c_{d,\ell}\, h^{2\ell-1}([D_n^\ell \pi_h v], [D_n^\ell \pi_h w])_{\mathcal{F}_{h,i}},$$

where $c_{d,\ell} > 0$ is a parameter and $\mathcal{F}_{h,i}$ is the set of interior faces in $\mathcal{T}_{h,i}$ which belongs to an element that intersect the boundary $\partial \Omega_i$ (see Figure 3(a)), and $D_\xi^\ell v$ denotes the contraction of ξ^ℓ and $\nabla^\ell v$.
- For each skeleton subdomain $\Omega_{0,k}$, $1 \leq k \leq N_0$, define the stabilization form

$$(3.47) \qquad s_{h,0,k}(v,w) = \sum_{\ell=1}^{p} c_{d-1,\ell}\, h^{2\ell}\big((D_\nu^\ell \pi_h v, D_\nu^\ell \pi_h w)_{\Omega_{0,k}}$$

$$(3.48) \qquad + ([D_n^\ell \pi_h v], [D_n^\ell \pi_h w])_{\mathcal{F}_{h,0,k}}\big),$$

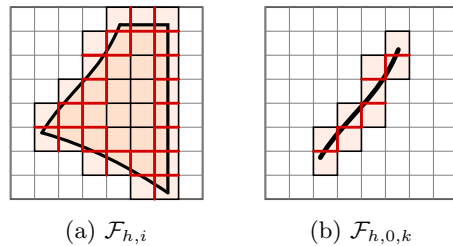(a) $\mathcal{F}_{h,i}$ (b) $\mathcal{F}_{h,0,k}$

Fig. 3. *Illustration of faces within the active meshes used in the stabilization forms. These faces are highlighted in red. (a) Faces for a subdomain Ω_i equipped with the active mesh $\mathcal{T}_{h,i}$. (b) Faces for a skeleton subdomain $\Omega_{0,k}$ equipped with the active mesh $\mathcal{T}_{h,0,k}$.*

where $c_{d-1,l} > 0$ is a parameter, ν is the normal to the smooth $d-1$ manifold $\Omega_{0,k}$, and $\mathcal{F}_{h,0,k}$ denotes the set of interior faces in $\mathcal{T}_{h,0,k}$; see Figure 3(b). These stabilization forms satisfy the abstract properties for stabilization forms specified in section 2.2. Proofs of these or very similar properties are given in, e.g., [33, 26, 31], but for completeness we below include proofs of the interpolation and consistency properties for the above forms.

Proof of interpolation properties (2.17) *and* (2.21). Since the definitions of the stabilization forms include the interpolation operator π_h, which is a projection, it trivially holds that $\|v - \pi_h v\|_{s_{h,i}} = 0$ and $\|v - \pi_h v\|_{s_{h,0,k}} = 0$.   □

Proof of consistency property (2.16). Let $v \in H^s(\Omega_i)$, $1 \le s \le p+1$. On every pair of adjoining elements $T_F^-, T_F^+ \in \mathcal{T}_{h,i}$ separated by a face $F \in \mathcal{F}_{h,i}$ we define an interpolant $\pi_F : H^1(T_F^- \cup T_F^+) \to \mathcal{P}^p(T_F^- \cup T_F^+)$, where $\mathcal{P}^p$ is the space of polynomials of degree less or equal to p, satisfying the standard interpolation estimate

$$(3.49) \qquad \|v - \pi_F v\|_{H^1(T_F^- \cup T_F^+)} \lesssim h^{s-1} \|v\|_{H^s(T_F^- \cup T_F^+)}.$$

To prove that (3.46) satisfies the interpolation property (2.17) we begin with

$$(3.50) \qquad s_{h,i}(\pi_h v, \pi_h v) = \sum_{\ell=1}^p c_{d,\ell}\, h^{2\ell-1} \sum_{F \in \mathcal{F}_{h,i}} \|[D_n^\ell \pi_h v]\|_F^2$$

$$(3.51) \qquad = \sum_{\ell=1}^p c_{d,\ell}\, h^{2\ell-1} \sum_{F \in \mathcal{F}_{h,i}} \|[D_n^\ell (\pi_h v - \pi_F v)]\|_F^2,$$

where we utilize that $[D_n^\ell \pi_F v]|_F = 0$ for all $F \in \mathcal{F}_{h,i}$ since $\pi_F v$ is a polynomial on each element pair. We now proceed as follows:

$$(3.52)\quad \|[D_n^\ell (\pi_h v - \pi_F v)]\|_F^2 \lesssim \|D_n^\ell ((\pi_h v)^+ - \pi_F v)\|_F^2 + \|D_n^\ell ((\pi_h v)^- - \pi_F v)\|_F^2$$

$$(3.53) \qquad\qquad\qquad \lesssim h^{-1} \|\pi_h v - \pi_F v\|_{H^\ell(T_F^+ \cup T_F^-)}^2$$

$$(3.54) \qquad\qquad\qquad \lesssim h^{1-2\ell} \|\pi_h v - \pi_F v\|_{H^1(T_F^+ \cup T_F^-)}^2$$

$$(3.55) \qquad\qquad\qquad \lesssim h^{1-2\ell} \left(\|\pi_h v - v\|_{H^1(T_F^+ \cup T_F^-)}^2 + \|v - \pi_F v\|_{H^1(T_F^+ \cup T_F^-)}^2 \right)$$

$$(3.56) \qquad\qquad\qquad \lesssim h^{2s-1-2\ell} \|v\|_{H^s(T_F^+ \cup T_F^-)}^2,$$

where we utilized the triangle inequality; applied inverse inequalities to move discrete functions first from the face onto a pair elements $T_F^+ \cup T_F^-$ and then down to $H^1(T_F^+ \cup T_F^-)$ norm; added and subtracted v and applied the triangle inequality; and finally, in () used interpolation estimates. In combination with (3.51) this concludes the proof. □

Proof of consistency property (2.20). Let $v \in H^{s-1/2}(\Omega_{0,k})$, $1 \le s \le p+1$. The skeleton stabilization form contains two parts, normal stabilization (3.47) and face stabilization (3.48), which we now consider separately.

Normal stabilization. Using inverse inequalities to move onto the tubular neighborhood $U_\delta(\Omega_{0,k})$ and a first order normal derivative we obtain

$$(3.57) \qquad h^{2\ell}\|D_\nu^\ell \pi_h v\|_{\Omega_{0,k}}^2 \lesssim \delta^{-1}h^{2\ell}\|D_\nu^\ell \pi_h v\|_{U_\delta(\Omega_{0,k})}^2$$

$$(3.58) \qquad\qquad \lesssim \delta^{-1}h^2\|D_\nu^1 \pi_h v\|_{U_\delta(\Omega_{0,k})}^2$$

$$(3.59) \qquad\qquad \lesssim \delta^{-1}h^2\|D_\nu^1 (\pi_h - I)E_{\Omega_{0,k}} v\|_{U_\delta(\Omega_{0,k})}^2$$

$$(3.60) \qquad\qquad \lesssim \delta^{-1}h^2\|(\pi_h - I)E_{\Omega_{0,k}} v\|_{H^1(U_\delta(\Omega_{0,k}))}^2$$

$$(3.61) \qquad\qquad \lesssim \delta^{-1}h^{2s-1}\|E_{\Omega_{0,k}} v\|_{H^{s-\frac{1}{2}}(U_\delta(\Omega_{0,k}))}^2$$

$$(3.62) \qquad\qquad \lesssim h^{2s-1}\|v\|_{H^{s-\frac{1}{2}}(\Omega_{0,k})}^2,$$

where in (3.59) we utilize that the extension is constant in the normal direction; in (3.61) use an interpolation estimate; and finally, in (3.31), use stability of the extension operator.

Face stabilization. Mimicking the computation (3.52)–(3.56) with an extended function $E_{\Omega_{0,k}} v \in H^{s-1/2}(U_\delta(\Omega_{0,k}))$, using the stability of the extension operator (3.31) and choosing $\delta \sim h$ yields the desired estimate.   □

3.4. Error estimates.

THEOREM 3.5 (energy norm error estimate). *The following estimate holds:*

$$(3.63) \qquad \|\|u - u_h\|\|_h^2 \lesssim h^{2p}\|u_0\|_{H^{p+1/2}(\Omega_0)}^2 + \sum_{i=1}^N h^{2p}\|u_i\|_{H^{p+1}(\Omega_i)}^2.$$

This result follows immediately from the coercivity; the weak Galerkin orthogonality (2.38); continuity; consistency of the stabilization forms (2.16) and (2.20); and an interpolation error estimate. For the reader's convenience we detail the proof.

Proof. Let $e_h = \pi_h u - u_h$ and $\rho = \pi_h u - u$. Then we have

$$(3.64) \qquad \|\|e_h\|\|_h^2 \lesssim A_h(e_h, e_h)$$

$$(3.65) \qquad\qquad = A_h(\rho, e_h) + s_h(u, e_h)$$

$$(3.66) \qquad\qquad \leq \|\|\rho\|\|_h \|\|e_h\|\|_h$$

$$(3.67) \qquad\qquad \lesssim \left(h^{2p}\|u_0\|_{H^{p+1/2}(\Omega_0)}^2 + \sum_{i=1}^N h^{2p}\|u_i\|_{H^{p+1}(\Omega_i)}^2 \right)^{1/2} \|\|e_h\|\|_h. \qquad □$$

Subdomain L2 error estimates. Assuming that the solution to the dual problem

$$(3.68) \qquad -\nabla \cdot a\nabla \phi = \psi \text{ in } \Omega, \qquad \phi = 0 \text{ on } \partial\Omega,$$

has the regularity

$$(3.69) \qquad \sum_{i=1}^N \|\phi_i\|_{H^s(\Omega_i)}^2 \lesssim \|\psi\|_\Omega^2, \qquad s \in (1, 3/2],$$

we have the following error estimate:

$$(3.70) \quad \sum_{i=1}^N \|u_i - u_{h,i}\|_{\Omega_i}^2 \lesssim h^{2p+2(s-1)}\|u_0\|_{H^{p+1/2}(\Omega_0)}^2 + \sum_{i=1}^N h^{2p+2(s-1)}\|u_i\|_{H^{p+1}(\Omega_i)}^2.$$

Skeleton L^2 error estimates. In order to estimate the L^2 norm of the skeleton error we instead consider the dual problem

$$-\nabla \cdot a_i \nabla \phi_i = 0 \qquad \text{in } \Omega_i, \tag{3.71}$$

$$[\![n \cdot a\nabla\phi]\!] = \psi \qquad \text{on } \Omega_0, \tag{3.72}$$

$$[\phi]_i = 0 \qquad \text{on } \partial\Omega_i \cap \Omega_0, \tag{3.73}$$

$$\phi_i = 0 \qquad \text{on } \partial\Omega_i \cap \partial\Omega \tag{3.74}$$

since ψ is in L^2 on the skeleton the maximal regularity is

$$\sum_{i=1}^{N} \|\phi_i\|_{H^{3/2}(\Omega_i)}^2 \lesssim \|\psi\|_{\Omega_0}^2 \tag{3.75}$$

and thus we arrive at the estimate

$$\|u_0 - u_{h,0}\|_{\Omega_0}^2 \lesssim h^{2p+1}\|u_0\|_{H^{p+1/2}(\Omega_0)}^2 + \sum_{i=1}^{N} h^{2p+1}\|u_i\|_{H^{p+1}(\Omega_i)}^2. \tag{3.76}$$

Observe that this shows that the error in the discrete $H^{1/2}$ norm, $h^{-\frac{1}{2}}\|u_0 - u_{h,0}\|$ has similar convergence order as the energy norm error, which is optimal.

4. The Schur complement. In this section we show how the bulk fields can be eliminated using the Schur complement and we derive a bound for the condition number of stiffness matrix associated with the Schur complement.

4.1. Definitions.
- Define the operator $T_h : V_{h,0} \to V_{h,1,N} = \bigoplus_{i=1}^{N} V_{h,i}$ such that

$$A_h(v_0 + T_h v_0, 0 \oplus w) = 0 \qquad \forall w \in V_{h,1,N}, \tag{4.1}$$

  where we used the notation $0 \oplus w$ to indicate that the component in $V_{h,0}$ is zero.
- Define the Schur complement form on $V_{h,0}$ by

$$S_h(v_0, w_0) = A_h(v_0 + T_h v_0, w_0 + T_h w_0), \qquad v_0, w_0 \in V_{h,0}. \tag{4.2}$$

- Define the energy norm on $V_{h,0}$ associated with the Schur complement by

$$|||v_0|||_{S_h} = |||v_0 + T_h v_0|||_h. \tag{4.3}$$

- It follows directly from the definition of the Schur complement form that S_h is coercive and continuous on $V_{h,0}$.

4.2. Solution using the Schur complement. Note that we have the A_h-orthogonal splitting

$$W_h = (I + T_h)V_{h,0} \perp (\{0\} \oplus V_{h,1,N}) \tag{4.4}$$

and thus $u_h = (I + T_h)u_{h,0} + (0 \oplus u_{h,1,N})$, where $u_{h,0} \in V_{h,0}$ is the solution to

$$S_h(u_{h,0}, v_0) = l_h((I + T_h)v_0) \qquad \forall v_0 \in V_{h,0} \tag{4.5}$$

and $u_{h,1,N}$ is the solution to

$$A_h(0 \oplus u_{h,1,N}, 0 \oplus v) = l_h(0 \oplus v) \qquad \forall v \in V_{h,1,N}. \tag{4.6}$$

We note that (4.6) decouples and can be solved subdomainwise. For each subdomain Ω_i, $1 \leq i \leq N$, we get a Nitsche type formulation with homogeneous Dirichlet data and right-hand side $f_i = f|_{\Omega_i}$.

4.3. Some basic estimates. We collect the basic bounds needed to show an estimate of the condition number of the stiffness matrix associated with the Schur complement.

LEMMA 4.1 (norm equivalence). *There are constants such that*

$$\text{(4.7)} \qquad \inf_{w \in V_{h,1,N}} \||v_0 + w\||_h \lesssim \||v_0\||_{S_h} \lesssim \inf_{w \in V_{h,1,N}} \||v_0 + w\||_h.$$

Proof. 1. By definition

$$\text{(4.8)} \qquad \inf_{w \in V_{h,1,N}} \||v_0 + w\||_h \lesssim \||v_0 + T_h v_0\||_h = \||v_0\||_{S_h}.$$

2. We have

$$\text{(4.9)} \qquad \||v_0\||^2_{S_h} = \||v_0 + T_h v_0\||^2_h$$
$$\text{(4.10)} \qquad \lesssim A_h(v_0 + T_h v_0, v_0 + T_h v_0)$$
$$\text{(4.11)} \qquad = A_h(v_0 + T_h v_0, v_0 + w)$$
$$\text{(4.12)} \qquad \lesssim \underbrace{\||v_0 + T_h v_0\||_h}_{=\||v_0\||_{S_h}} \||v_0 + w\||_h,$$

where we used the coercivity (3.3) of A_h, the orthogonality (4.1) of T_h, and the continuity (3.2) of A_h. Thus we conclude that

$$\text{(4.13)} \qquad \||v_0\||_{S_h} \lesssim \||v_0 + w\||_h$$

for all $w \in V_{h,1,N}$, and therefore

$$\text{(4.14)} \qquad \||v_0 + T_h v_0\||_h \lesssim \inf_{w \in V_{h,1,N}} \||v_0 + w\||_h. \qquad \square$$

LEMMA 4.2 (skeleton Poincaré estimate). *There is a constant such that for all* $v \in V_{h,0}$,

$$\text{(4.15)} \qquad \Big(\min_{1 \le i \le N} d_{\Omega_i} \Big) h^{-1} \|v\|^2_{\mathcal{T}_{h,0}} \lesssim \||v\||^2_{S_h}.$$

Proof. Using the Poincaré inequality (3.30) we have for any $w \in V_{h,1,N}$

$$\text{(4.16)} \qquad \Big(\min_{1 \le i \le N} d_{\Omega_i} \Big) h^{-1} \|v\|^2_{\mathcal{T}_{h,0}} \lesssim \||v + w\||^2_h$$

and as a consequence

$$\text{(4.17)} \qquad \Big(\min_{1 \le i \le N} d_{\Omega_i} \Big) h^{-1} \|v\|^2_{\mathcal{T}_{h,0}} \lesssim \||v + T_h v\||^2_h = \||v\||^2_{S_h}. \qquad \square$$

LEMMA 4.3 (skeleton inverse estimate). *There is a constant such that for all* $v \in V_{h,0}$,

$$\text{(4.18)} \qquad \||v\||^2_{S_h} \lesssim h^{-2} \|v\|_{\mathcal{T}_{h,0}}.$$

Proof. We have

$$
\begin{align}
(4.19) \qquad \|\|v_0\|\|_{S_h}^2 &\lesssim \inf_{w \in V_{h,1,N}} \|\|v_0 + w\|\|_h^2 \\
(4.20) \qquad &\lesssim \|\|v_0 \oplus 0\|\|_h^2 \\
(4.21) \qquad &= \sum_{i=1}^N h^{-1}\|v_0\|_{\partial\Omega_i}^2 + \|v\|_{s_{h,0}}^2 \\
(4.22) \qquad &\lesssim h^{-1}(\|v_0\|_{\Omega_0}^2 + \|v_0\|_{s_{h,0}}^2) \\
(4.23) \qquad &\lesssim h^{-2}\|v_0\|_{\mathcal{T}_{h,0}},
\end{align}
$$

where we choose $w = 0$ on $V_{h,1,N}$, use the definition of the energy norm, and finally employ the inverse estimate (2.22). □

4.4. Condition number estimate for the Schur complement.

Definitions and basic results.

- Let $\{\varphi_i\}_{i=1}^D$ be the basis in $V_{h,0}$ and denote the expansion by

$$
(4.24) \qquad v = \sum_{i=1}^D \widehat{v}_i \varphi_i.
$$

  Then we have the equivalence

$$
(4.25) \qquad \|v\|_{\mathcal{T}_{h,0}}^2 \sim h^d \|\widehat{v}\|_{\mathbb{R}^D}^2.
$$

- The stiffness matrix associated with the Schur complement is defined by

$$
(4.26) \qquad (\widehat{S}\widehat{v}, \widehat{w})_{\mathbb{R}^D} = S_h(v, w).
$$

  Then $\widehat{S}$ is symmetric positive definite and thus the spectrum is real and positive, and we have the Rayleigh quotient characterization of the largest and smallest eigenvalues

$$
(4.27) \qquad \lambda_{\max} = \max_{\widehat{v} \in \mathbb{R}^D \setminus \{0\}} \frac{(\widehat{S}\widehat{v}, \widehat{v})_{\mathbb{R}^D}}{\|\widehat{v}\|_{\mathbb{R}^D}^2}, \qquad \lambda_{\min} = \min_{\widehat{v} \in \mathbb{R}^D \setminus \{0\}} \frac{(\widehat{S}\widehat{v}, \widehat{v})_{\mathbb{R}^D}}{\|\widehat{v}\|_{\mathbb{R}^D}^2}.
$$

- The condition number is defined by

$$
(4.28) \qquad \kappa = \frac{\lambda_{\max}}{\lambda_{\min}},
$$

  where $\lambda_{\max}$ and $\lambda_{\min}$ denote the maximum and minimum eigenvalues of $\widehat{S}$. In view of (4.27) we have the identity

$$
(4.29) \qquad \kappa = \max_{\widehat{v} \in \mathbb{R}^D \setminus \{0\}} \frac{(\widehat{S}\widehat{v}, \widehat{v})_{\mathbb{R}^D}}{\|\widehat{v}\|_{\mathbb{R}^D}^2} \max_{\widehat{v} \in \mathbb{R}^D \setminus \{0\}} \frac{\|\widehat{v}\|_{\mathbb{R}^D}^2}{(\widehat{S}\widehat{v}, \widehat{v})_{\mathbb{R}^D}}.
$$

THEOREM 4.4 (condition number estimate). *The condition number satisfies the estimate*

$$
(4.30) \qquad \kappa(\widehat{S}) \lesssim h^{-1}\Big(\min_{1 \leq i \leq N} d_{\Omega_i}\Big)^{-1}.
$$

Proof. The bound follows directly from the following two estimates:

1. We have

$$(4.31) \qquad (\widehat{S}\widehat{v}, \widehat{v})_{\mathbb{R}^D} = A_h(v + T_h v, v + T_h v)$$

$$(4.32) \qquad \lesssim \||v + T_h v\||_h^2$$

$$(4.33) \qquad = \||v\||_{S_h}^2$$

$$(4.34) \qquad \lesssim h^{-2}\|v\|_{\mathcal{T}_{h,0}}^2$$

$$(4.35) \qquad \lesssim h^{-2}h^d\|\widehat{v}\|_{\mathbb{R}^D}^2,$$

where we used the continuity (3.2) of A_h, the skeleton inverse estimate (4.18), and the equivalence (4.25). Thus we conclude that

$$(4.36) \qquad \lambda_{\max} \lesssim h^{d-2}.$$

2. We have

$$(4.37) \qquad (\widehat{S}\widehat{v}, \widehat{v})_{\mathbb{R}^D} = A_h(v + T_h v, v + T_h v)$$

$$(4.38) \qquad \gtrsim \||v + T_h v\||_h^2$$

$$(4.39) \qquad \gtrsim \Big(\min_{1 \leq i \leq N} d_{\Omega_i} \Big) h^{-1}\|v\|_{L^2(\mathcal{T}_{h,0})}^2$$

$$(4.40) \qquad \gtrsim \Big(\min_{1 \leq i \leq N} d_{\Omega_i} \Big) h^{-1}h^d\|\widehat{v}\|_{\mathbb{R}^D}^2,$$

where we used the coercivity (3.3) of A_h, the Poincaré estimate (4.15), and the equivalence (4.25). We conclude that

$$(4.41) \qquad \lambda_{\min}^{-1} \lesssim h^{-(d-1)}\Big(\min_{1 \leq i \leq N} d_{\Omega_i} \Big)^{-1}. \qquad \square$$

5. Numerical results. For assessment and illustration we implemented a two-dimensional version of the method. We first give some details on implementation choices and then we present some illustrating examples and convergence results.

5.1. Implementation. Our implementation extend upon the implementation detailed in [28] for problems on parametric multipatch surfaces to the hybridized case, albeit constrained to two dimensions and without parametric mappings.

Approximation spaces. On each subdomain and skeleton subdomain we define an approximation space by a mesh equipped with some finite elements. In all examples below we use standard Lagrange elements of degree p which on quadrilaterals are tensor product polynomial elements Q_p and on triangles are full polynomial elements P_p. While the mesh on each subdomain and skeleton subdomain could be constructed completely independently of each other we here focus on two cases:

- *Global background grid.* All meshes, i.e., subdomain meshes $\{\mathcal{T}_{h,i}\}_{i=1}^N$ and skeleton subdomain meshes $\{\mathcal{T}_{h,0,k}\}_{k=1}^{N_0}$, are extracted from the same background grid $\mathcal{T}_{h,\Omega}$.
- *Single element interfaces.* Subdomain meshes $\{\mathcal{T}_{h,i}\}_{i=1}^N$ may be arbitrarily constructed while each skeleton subdomain $\Omega_{0,k}$, $1 \leq k \leq N_0$, is equipped with a mesh $\mathcal{T}_{h,0,k}$ consisting of a single, typically higher order, element in $\mathbb{R}^d$.

The benefit of either choice is that the implementation of the Nitsche terms, i.e., the patch boundary terms in (2.32)–(2.34), becomes particularly straightforward as for

$T \in \mathcal{T}_{h,i}$, $\partial\Omega_i \cap T \neq \emptyset$, we trivially know the corresponding element in the skeleton subdomain mesh and that $\partial\Omega_i \cap T$ is completely contained within that element. More general cases require the construction of the union of subdomain meshes and skeleton subdomain meshes to correctly evaluate the skeleton integrals. For curved skeletons, parametrically mapped subdomains, or simply the case $d = 3$ this construction is challenging to perform in a robust and efficient manner. An attractive feature of the global background grid is that it readily gives an optimal order method, a feature which we typically do not have using single element interfaces without adapting the skeleton element order. Instead, the attractive feature of single element interfaces is that the simple implementation also covers cases when subdomain meshes do not match over the skeleton.

Parameter choices. For the Nitsche penalty parameter we choose $\beta = 20 \cdot p^2$ and for the stabilization parameters we, similarly to the numerical examples in [31], choose $c_{d,\ell} = c_{d-1,\ell} = \frac{10^{-2}}{\ell!}$. We note no particular sensitivity in the choice of values for these parameters.

5.2. Numerical examples. For our numerical examples we consider different partitions of the unit square $[0,1]^2$. We let the right-hand side be given by $f = 1$ and we vary the material coefficient a in each subdomain.

Example 1: *Three subdomains.* For our first numerical example we partition the unit square into three subdomains with a different constant material coefficient $a \in \{1, 2, 3\}$ in each subdomain; see Figure 4. Thus, we in this problem have three skeleton subdomains. We consider both of the mesh constructions described in section 5.1:

- *Global background grid.* Here all meshes are extracted from the same background grid (see Figure 5), and we use Q_2 elements on each mesh. Note that all subdomains have cut elements and that some skeleton subdomains are curved within elements. In this setting there are no locking effects due to nonmatching approximation spaces when choosing the penalty parameter β large. A sample solution and the magnitude of its gradient are presented in Figure 6.
- *Single element interfaces.* Here the mesh on each subdomain is constructed independently, some as quadrilateral meshes and some as triangular, and we equip all subdomain meshes with Q_2/P_2 elements. On each skeleton subdomain we use a single Q_4 element. Sample meshes in this set-up are visualized in Figure 7 and the corresponding numerical solution is presented in Figure 8.

Example 2: *Voronoi diagram.* In our second example we construct a subdivision of the unit square by generating a Voronoi diagram from 50 uniformly distributed; random points in $[0,1]^2$ and taking the restriction of this diagram to the unit square;
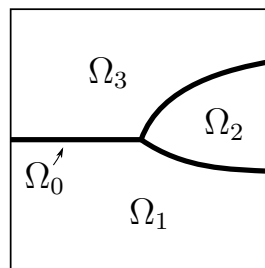

FIG. 4. *Illustrations of the model problem geometry. The unit square $[0,1]^2$ is divided into three subdomains according to the figure with material coefficients $a_1 = 1$, $a_2 = 2$, and $a_3 = 3$.*
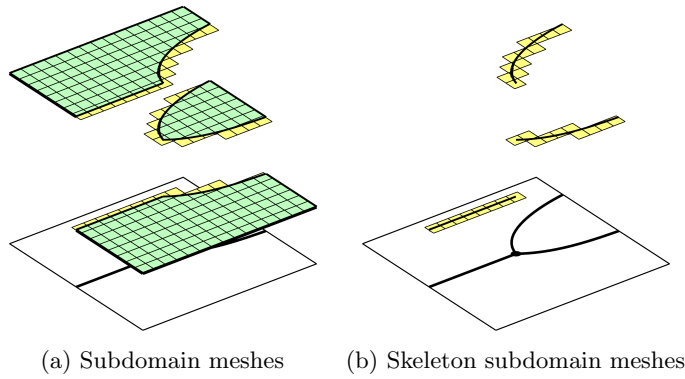
(a) Subdomain meshes   (b) Skeleton subdomain meshes

FIG. 5. *Meshes in the three subdomains example extracted from a global background grid.* (a) *Subdomain solutions are approximated using Q_2 elements.* (b) *Skeleton subdomain solutions are approximated in an embedding space of Q_2 elements.*
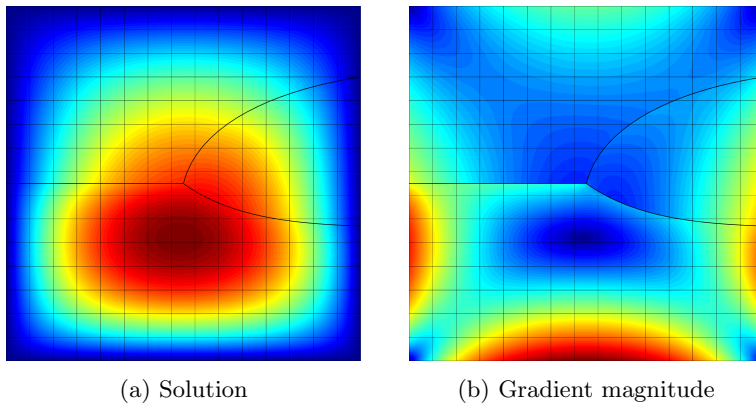

(a) Solution   (b) Gradient magnitude

FIG. 6. *Three subdomains with different material coefficients and Q_2 meshes extracted from a global background grid.*

(a) Subdomain meshes   (b) Skeleton subdomain meshes
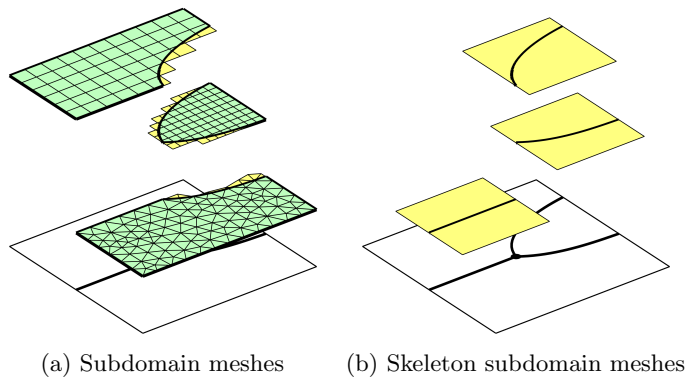
FIG. 7. *Meshes in the three subdomains example with skeleton subdomains embedded in a single element.* (a) *Subdomain solutions are approximated using Q_2 and P_2 elements on quadrilateral, respectively, triangle, meshes.* (b) *Each skeleton subdomain is embedded in a single Q_4 element.*

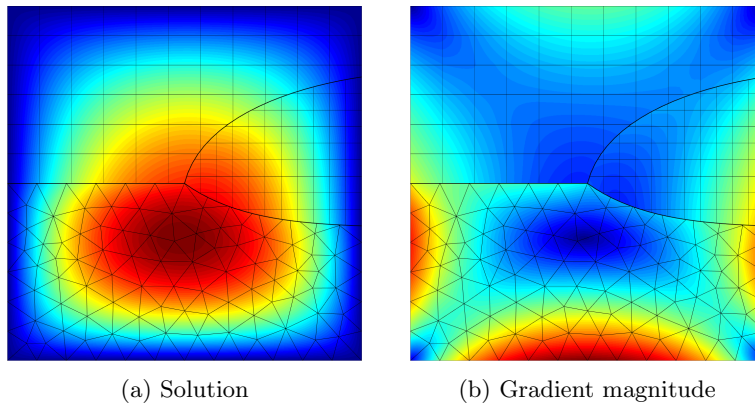(a) Solution   (b) Gradient magnitude

FIG. 8. *Three subdomains with different material coefficients and nonmatching meshes. Here meshes with Q_2/P_2 elements are used on each subdomain. On each skeleton subdomain the solution is approximated using a single Q_4 element.*
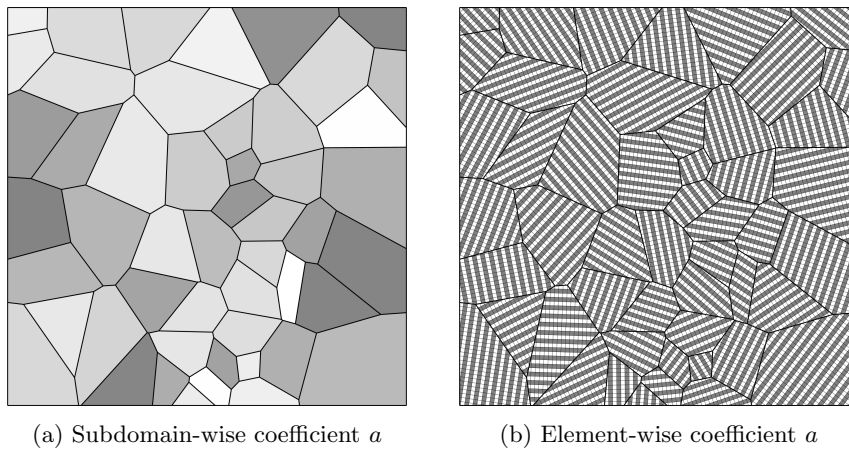

(a) Subdomain-wise coefficient a (b) Element-wise coefficient a

FIG. 9. *Subdivisions of the unit square $[0,1]^2$ generated from Voronoi diagrams featuring varying material coefficients. (a) Domain with material coefficient $a \in [0.01, 1]$ which is constant within each subdomain and chosen using a uniformly distributed random variable. (b) Domain with a randomly oriented mesh in each subdomain and a material coefficient a which alternates between 1 and 1000 rowwise in the mesh.*

see Figure 9. We again consider the two different set-ups regarding mesh construction, although we make different choices for the material coefficient in the two cases.

- *Global background grid.* Here we extract all meshes from the same background grid and we equip our meshes with Lagrange Q_2 elements. The material coefficient is constant on each subdomain Ω_i and is chosen as $a_i = 0.01 + X$, where $X \in [0, 1]$ is a uniformly distributed random variable. This set-up is illustrated in Figure 9(a). We can easily generate background grids of any mesh size and in Figure 10 we present results for three different mesh sizes. In Figures 10(c)–10(d) we note that the method also works well when the mesh size is of the same order as the subdomain sizes. The extreme case where we only have a single element on each subdomain is presented
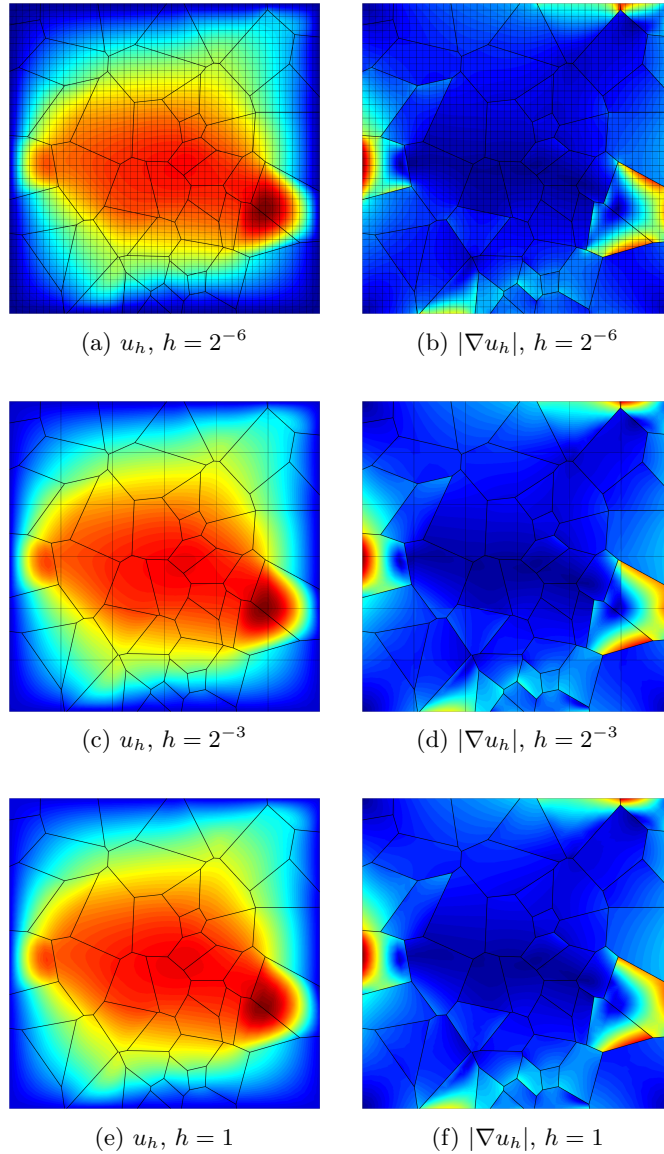
(a) u_h, $h = 2^{-6}$

(b) $|\nabla u_h|$, $h = 2^{-6}$

(c) u_h, $h = 2^{-3}$

(d) $|\nabla u_h|$, $h = 2^{-3}$

(e) u_h, $h = 1$

(f) $|\nabla u_h|$, $h = 1$

FIG. 10. *Numerical solution u_h and gradient magnitude $|\nabla u_h|$ on a Voronoi diagram subdivision with subdomainwise constant material coefficient; see Figure 9(a). (a)–(b) Q_2 elements on meshes generated from one fine grid. (c)–(d) Q_2 elements on meshes generated from one coarse grid with a mesh size in the same order as the subdomain sizes. (e)–(f) A single Q_2 element on each subdomain and skeleton subdomain.*

in Figures 10(e)–10(f). This is much like a hybridized version of so-called polygonal/polyhedral elements; see the overview in [14]. Note that in this extreme case we construct the single elements such that they are as small as possible while still containing its subdomain to avoid conditioning problems.

- *Single element interfaces.* In the situation where we equip each skeleton subdomain with a single Lagrange Q_4 element we choose another set-up regarding
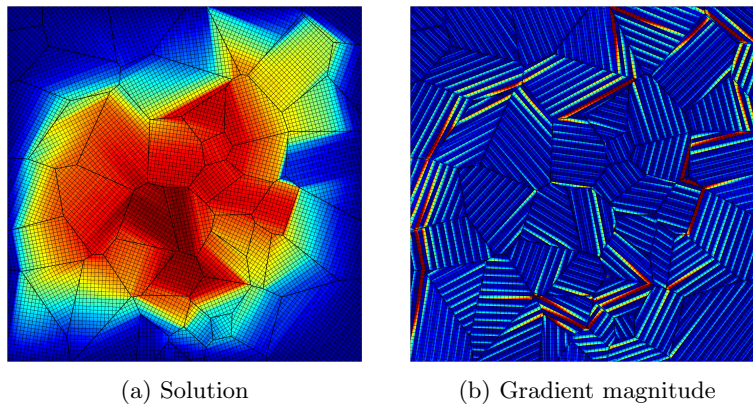
(a) Solution   (b) Gradient magnitude

FIG. 11. *Numerical solution u_h and gradient magnitude $|\nabla u_h|$ on a Voronoi diagram subdivision with a fine scale material coefficient pattern. On each subdomain a randomly oriented Q_2 mesh with a rowwise alternating material coefficient is set up; see Figure 9(b). The numerical solution on each skeleton subdomain is instead approximated by a single Q_4 element.*

meshes and material coefficient in each bulk subdomain. We randomly position a fine mesh equipped with Lagrange Q_2 elements on each subdomain and we let the material coefficient alternate between 1 and 1000 rowwise in the mesh. This set-up is illustrated in Figure 9(b) and the numerical solution is presented in Figure 11. Note that this case is mainly an illustration of how we conveniently can implement cases where the subdomains are defined via mappings, in this case a rotation. Of course we here lose fine scale information across the skeleton and we have made no special adaption to handle the large variation in the material coefficient.

5.3. Convergence and stability.

Convergence studies. To study the convergence of the method in energy and L^2 norms we let Ω be the upper left quarter of the unit circle and partition this domain into two parts, in polar coordinates (r, ϕ) defined $\Omega_1 = \{0 < r < \frac{2}{3}, \ 0 < \phi < \frac{\pi}{2}\}$ and $\Omega_2 = \{\frac{2}{3} < r < 1, \ 0 < \phi < \frac{\pi}{2}\}$. Each of the two arcs in this domain is discretized using 3600 linear segments. We manufacture a problem with known exact solution from the ansatz

$$(5.1) \qquad u = \left\{ u_0 = \frac{2^2}{3^2} \sin(2\phi), \ u_1 = r^2 \sin(2\phi), \ u_2 = \frac{2^3}{3^2\sqrt{3}} \sin(2\pi r)\sin(2\phi) \right\}$$

with coefficients $a_1 = 2\pi$, $a_2 = 3\sqrt{3}$. The domain, exact solution and exact gradient magnitude for this problem are displayed in Figure 12.

- *Global background grid.* In Figure 13 we present convergence results in the case where all meshes are extracted from the same quadrilateral background grid using Q_p elements, $p = 1, 2, 3$, and we achieve the expected convergence rates of $O(h^p)$ and $O(h^{p+1})$ in the energy and the L^2 norm, respectively. We attribute the loss of convergence eventually appearing for Q_3 elements in the L^2 norm to the fixed geometry approximation using high resolution polygons.
- *Single element interfaces.* In this case we instead use Q_2 elements of size h on each subdomain but only a single Lagrange Q_p element, $p = 2, 4, 6$, on

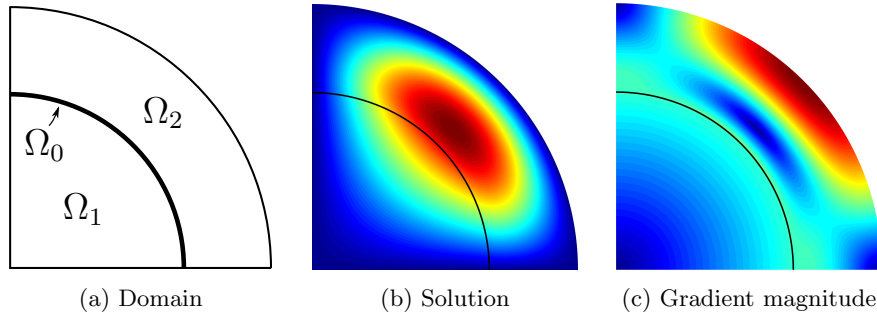(a) Domain   (b) Solution   (c) Gradient magnitude

FIG. 12. *Problem with known exact solution used in convergence studies.* (a) *The domain is the upper right quarter of the unit circle partitioned at a distance 2/3 from the corner.* (b) *The exact solution* (5.1). (c) *The gradient magnitude of the exact solution.*
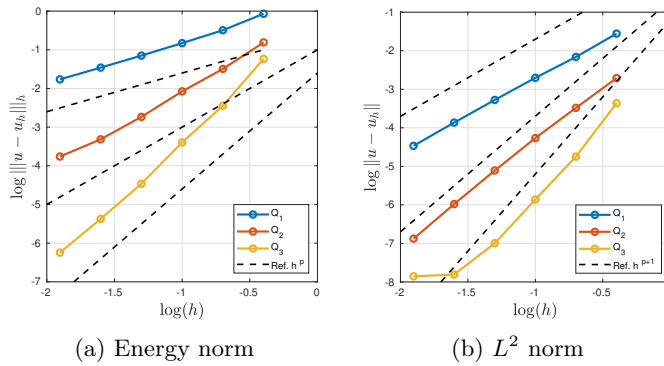

(a) Energy norm   (b) L^2 norm

FIG. 13. *Convergence studies using meshes all from the same background grid. In all meshes the same elements are used (Q_1–Q_3) and we achieve what we expect to be optimal convergence rates of* (a) $O(h^p)$ *in the energy norm, respectively,* (b) $O(h^{p+1})$ *in the L^2 norm. The curved geometry is approximated as a fixed high resolution polygon, which explains why we see the L^2 error eventually leveling off for the highest order element.*

each skeleton subdomain. As the skeleton subdomain meshes are not refined with smaller h this naturally imposes a lower bound on the errors, which we also note in the convergence results presented in Figure 14.

Condition number bound. To illustrate how the bound on the condition number for the stiffness matrix associated with the Schur complement scales with the mesh size, as shown in Theorem 4.4, we estimate the condition number in the case of the model problem with three subdomains illustrated in Figure 4. The results are shown in Figure 15, where we use global background grids with Q_1, respectively, Q_2, elements. To produce a variety of cut situations for the elements in our mesh, for each mesh size we repeat the experiment 20 times using random positions for the background grid. As shown, there is significant variance of the condition number but with a stable trend of $O(h^{-1})$ as implied by our bound in Theorem 4.4.
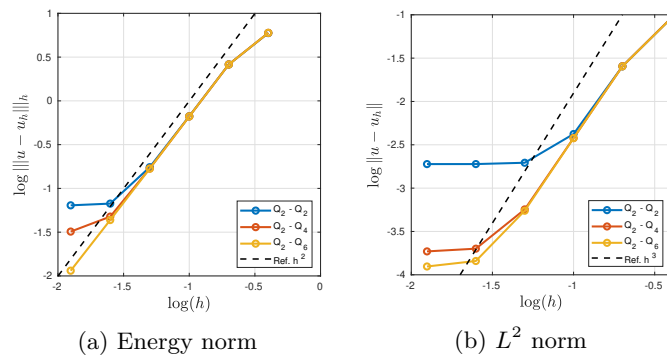
(a) Energy norm (b) L^2 norm

FIG. 14. *Convergence studies using nonmatching meshes for the subdomains and a single polynomial for each skeleton subdomain. On the subdomains Q_2 elements are used and on the skeleton subdomains Q_2–Q_6 polynomials are used. Because there is no h refinement of the skeleton subdomains the convergence levels out as the polynomial approximations on the skeleton become the dominant source of error.*
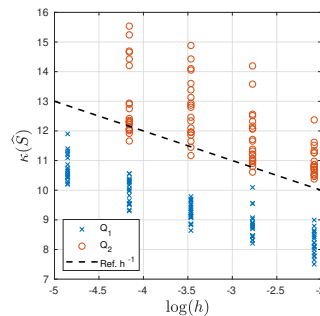

FIG. 15. *Study of how the condition number for the stiffness matrix associated with the Schur complement scales with the mesh size in the case of using a global background grid in Example 1 as illustrated in Figure 6. For each mesh size the experiment is repeated 20 times with random position of the background grid creating a variety of cut situations. To make sure we were in the asymptotic regime, for this experiment we increased the skeleton stabilization parameter to $c_{d-1,\ell} = \frac{1}{\ell!}$.*

REFERENCES

[1] L. BEIRÃO DA VEIGA, F. BREZZI, L. D. MARINI, AND A. RUSSO, *The hitchhiker's guide to the virtual element method*, Math. Models Methods Appl. Sci., 24 (2014), pp. 1541–1573, https://doi.org/10.1142/S021820251440003X.

[2] S. P. A. BORDAS, E. BURMAN, M. G. LARSON, AND M. A. OLSHANSKII, EDS., *Geometrically Unfitted Finite Element Methods and Applications*, Lect. Notes Comput. Sci. Eng. 121, Springer, New York, 2017, https://doi.org/10.1007/978-3-319-71431-8.

[3] E. BURMAN, *Ghost penalty*, C. R. Math. Acad. Sci. Paris, 348 (2010), pp. 1217–1220, https://doi.org/10.1016/j.crma.2010.10.006.

[4] E. BURMAN, S. CLAUS, P. HANSBO, M. G. LARSON, AND A. MASSING, *CutFEM: Discretizing geometry and partial differential equations*, Internat. J. Numer. Methods Engrg., 104 (2015), pp. 472–501, https://doi.org/10.1002/nme.4823.

[5] E. BURMAN, D. ELFVERSON, P. HANSBO, M. G. LARSON, AND K. LARSSON, *A cut finite element method for the Bernoulli free boundary value problem*, Comput. Methods Appl. Mech. Engrg., 317 (2017), pp. 598–618, https://doi.org/10.1016/j.cma.2016.12.021.

[6] E. BURMAN, D. ELFVERSON, P. HANSBO, M. G. LARSON, AND K. LARSSON, *Shape optimization using the cut finite element method*, Comput. Methods Appl. Mech. Engrg., 328 (2018), pp. 242–261, https://doi.org/10.1016/j.cma.2017.09.005.

[7] E. Burman and P. Hansbo, *Fictitious domain finite element methods using cut elements:* II. *A stabilized Nitsche method*, Appl. Numer. Math., 62 (2012), pp. 328–341, https://doi.org/10.1016/j.apnum.2011.01.008.

[8] E. Burman, P. Hansbo, and M. G. Larson, *A stabilized cut finite element method for partial differential equations on surfaces: The Laplace-Beltrami operator*, Comput. Methods Appl. Mech. Engrg., 285 (2015), pp. 188–207, https://doi.org/10.1016/j.cma.2014.10.044.

[9] E. Burman, P. Hansbo, and M. G. Larson, *A cut finite element method with boundary value correction*, Math. Comp., 87 (2018), pp. 633–657, https://doi.org/10.1090/mcom/3240.

[10] E. Burman, P. Hansbo, and M. G. Larson, *Low Regularity Estimates for CutFEM Approximations of an Elliptic Problem with Mixed Boundary Conditions*, Tech. report, Mathematics, Umeå University, Sweden, 2018.

[11] E. Burman, P. Hansbo, M. G. Larson, and K. Larsson, *Cut finite elements for convection in fractured domains*, Comput. & Fluids, 179 (2019), pp. 726–734, https://doi.org/10.1016/j.compfluid.2018.07.022.

[12] E. Burman, P. Hansbo, M. G. Larson, and A. Massing, *Cut finite element methods for partial differential equations on embedded manifolds of arbitrary codimensions*, ESAIM Math. Model. Numer. Anal., 52 (2018), pp. 2247–2282, https://doi.org/10.1051/m2an/2018038.

[13] A. Cangiani, Z. Dong, E. H. Georgoulis, and P. Houston, *hp-Version Discontinuous Galerkin Methods on Polygonal and Polyhedral Meshes*, SpringerBriefs in Math., Springer, New York, 2017, https://doi.org/10.1007/978-3-319-67673-9.

[14] A. Cangiani, E. H. Georgoulis, and P. Houston, *hp-version discontinuous Galerkin methods on polygonal and polyhedral meshes*, Math. Models Methods Appl. Sci., 24 (2014), pp. 2009–2041, https://doi.org/10.1142/S0218202514500146.

[15] B. Cockburn, D. A. Di Pietro, and A. Ern, *Bridging the hybrid high-order and hybridizable discontinuous Galerkin methods*, ESAIM Math. Model. Numer. Anal., 50 (2016), pp. 635–650, https://doi.org/10.1051/m2an/2015051.

[16] B. Cockburn, J. Gopalakrishnan, and R. Lazarov, *Unified hybridization of discontinuous Galerkin, mixed, and continuous Galerkin methods for second order elliptic problems*, SIAM J. Numer. Anal., 47 (2009), pp. 1319–1365, https://doi.org/10.1137/070706616.

[17] D. A. Di Pietro, A. Ern, and S. Lemaire, *An arbitrary-order and compact-stencil discretization of diffusion on general meshes based on local reconstruction operators*, Comput. Methods Appl. Math., 14 (2014), pp. 461–472, https://doi.org/10.1515/cmam-2014-0018.

[18] H. Egger, *A Class of Hybrid Mortar Finite Element Methods for Interface Problems with Non-matching Meshes*, preprint, AICES-2009-2, 2009.

[19] H. Egger and J. Schöberl, *A hybrid mixed discontinuous Galerkin finite-element method for convection-diffusion problems*, IMA J. Numer. Anal., 30 (2010), pp. 1206–1234, https://doi.org/10.1093/imanum/drn083.

[20] H. Egger and C. Waluga, *A hybrid mortar method for incompressible flow*, Int. J. Numer. Anal. Model., 9 (2012), pp. 793–812, https://doi.org/10.1007/s10596-011-9259-x.

[21] H. Egger and C. Waluga, *hp analysis of a hybrid DG method for Stokes flow*, IMA J. Numer. Anal., 33 (2013), pp. 687–721, https://doi.org/10.1093/imanum/drs018.

[22] J. Grande, C. Lehrenfeld, and A. Reusken, *Analysis of a high-order trace finite element method for PDEs on level set surfaces*, SIAM J. Numer. Anal., 56 (2018), pp. 228–255, https://doi.org/10.1137/16M1102203.

[23] A. Hansbo and P. Hansbo, *An unfitted finite element method, based on Nitsche's method, for elliptic interface problems*, Comput. Methods Appl. Mech. Engrg., 191 (2002), pp. 5537–5552, https://doi.org/10.1016/S0045-7825(02)00524-8.

[24] A. Hansbo, P. Hansbo, and M. G. Larson, *A finite element method on composite grids based on Nitsche's method*, ESAIM Math. Model. Numer. Anal., 37 (2003), pp. 495–514, https://doi.org/10.1051/m2an:2003039.

[25] P. Hansbo, T. Jonsson, M. G. Larson, and K. Larsson, *A Nitsche method for elliptic problems on composite surfaces*, Comput. Methods Appl. Mech. Engrg., 326 (2017), pp. 505–525, https://doi.org/10.1016/j.cma.2017.08.033.

[26] P. Hansbo, M. G. Larson, and K. Larsson, *Cut finite element methods for linear elasticity problems*, in Geometrically Unfitted Finite Element Methods and Applications, Lect. Notes Comput. Sci. Eng. 121, Springer, New York, 2017, pp. 25–63, https://doi.org/10.1007/978-3-319-71431-8_2.

[27] J. Haslinger and R. A. E. Mäkinen, *Introduction to Shape Optimization: Theory, Approximation, and Computation*, Adv. Des. Control 7, SIAM, Philadelphia, 2003, https://doi.org/10.1137/1.9780898718690.

[28] T. Jonsson, M. G. Larson, and K. Larsson, *Cut finite element methods for elliptic problems on multipatch parametric surfaces*, Comput. Methods Appl. Mech. Engrg., 324 (2017), pp. 366–394, https://doi.org/10.1016/j.cma.2017.06.018.

[29] R. B. Kellogg, *On the Poisson equation with intersecting interfaces*, Appl. Anal., 4 (1974), pp. 101–129, https://doi.org/10.1080/00036817408839086.

[30] J. Könnö and R. Stenberg, *Numerical computations with H(div)-finite elements for the Brinkman problem*, Comput. Geosci., 16 (2012), pp. 139–158, https://doi.org/10.1007/s10596-011-9259-x.

[31] M. G. Larson and S. Zahedi, *Stabilization of higher order cut finite element methods on surfaces*, IMA J. Numer. Anal., to appear, https://doi.org/10.1093/imanum/drz021.

[32] C. Lehrenfeld and A. Reusken, *Analysis of a high-order unfitted finite element method for elliptic interface problems*, IMA J. Numer. Anal., 38 (2018), pp. 1351–1387, https://doi.org/10.1093/imanum/drx041.

[33] A. Massing, M. G. Larson, A. Logg, and M. E. Rognes, *A stabilized Nitsche fictitious domain method for the Stokes problem*, J. Sci. Comput., 61 (2014), pp. 604–628, https://doi.org/10.1007/s10915-014-9838-9.

[34] M. Miyashita and N. Saito, *Hybridized discontinuous Galerkin method for elliptic interface problems: Error estimates under low regularity assumptions of solutions*, J. Sci. Comput., 76 (2018), pp. 1657–1673, https://doi.org/10.1007/s10915-018-0678-x.

[35] I. Oikawa and F. Kikuchi, *Discontinuous Galerkin FEM of hybrid type*, JSIAM Lett., 2 (2010), pp. 49–52, https://doi.org/10.14495/jsiaml.2.49.

[36] M. A. Olshanskii, A. Reusken, and J. Grande, *A finite element method for elliptic equations on surfaces*, SIAM J. Numer. Anal., 47 (2009), pp. 3339–3358, https://doi.org/10.1137/080717602.

[37] A. Reusken, *Analysis of trace finite element methods for surface partial differential equations*, IMA J. Numer. Anal., 35 (2015), pp. 1568–1590, https://doi.org/10.1093/imanum/dru047.

[38] L. R. Scott and S. Zhang, *Finite element interpolation of nonsmooth functions satisfying boundary conditions*, Math. Comp., 54 (1990), pp. 483–493, https://doi.org/10.2307/2008497.

[39] C. H. Villanueva and K. Maute, *CutFEM topology optimization of 3D laminar incompressible flow problems*, Comput. Methods Appl. Mech. Engrg., 320 (2017), pp. 444–473, https://doi.org/10.1016/j.cma.2017.03.007.